Remote Sens. **2015**, *7*, 6862-6885; doi:10.3390/rs70606862

OPEN ACCESS

remote sensing

ISSN 2072-4292

www.mdpi.com/journal/remotesensing

Article

Leaf Area Index Retrieval Combining HJ1/CCD and Landsat8/OLI Data in the Heihe River Basin, China

Jing Zhao [1,2], Jing Li [1,2,*], Qinhuo Liu [1,2,*], Wenjie Fan [3], Bo Zhong [1,2], Shanlong Wu [1,2], Le Yang [1,2], Yelu Zeng [1,2,4], Baodong Xu [1,2,4] and Gaofei Yin [1,2,4]

[1] State Key Laboratory of Remote Sensing Science, Institute of Remote Sensing and Digital Earth, Chinese Academy of Sciences, Beijing 100101, China; E-Mails: zhaojing1@radi.ac.cn (J.Z.); zhongbo@radi.ac.cn (B.Z.); wsl0579@163.com (S.W.); yangle@radi.ac.cn (L.Y.); zengyelu@163.com (Y.Z.); xubd@radi.ac.cn (B.X.); coffing@163.com (G.Y)

[2] Joint Center for Global Change Studies, Beijing 100875, China

[3] Institute of Remote Sensing and GIS, Peking University, Beijing 100871, China; E-Mail: fanwj@pku.edu.cn

[4] College of Resources and Environment, University of Chinese Academy of Sciences, Beijing 100049, China

* Authors to whom correspondence should be addressed; E-Mails: lijing01@radi.ac.cn (J.L.), liuqh@radi.ac.cn (Q.L.); Tel./Fax: +86-010-6485-1880 (J.L.).

Academic Editors: Xin Li, Yuei-An Liou, Alfredo R. Huete and Prasad S. Thenkabail

Received: 18 February 2015 / Accepted: 15 May 2015 / Published: 28 May 2015

Abstract: The primary restriction on high resolution remote sensing data is the limit observation frequency. Using a network of multiple sensors is an efficient approach to increase the observations in a specific period. This study explores a leaf area index (LAI) inversion method based on a 30 m multi-sensor dataset generated from HJ1/CCD and Landsat8/OLI, from June to August 2013 in the middle reach of the Heihe River Basin, China. The characteristics of the multi-sensor dataset, including the percentage of valid observations, the distribution of observation angles and the variation between different sensor observations, were analyzed. To reduce the possible discrepancy between different satellite sensors on LAI inversion, a quality control system for the observations was designed. LAI is retrieved from the high quality of single-sensor observations based on a look-up table constructed by a unified model. The averaged LAI inversion over a 10-day period is set as the synthetic LAI value. The percentage of valid LAI inversions increases significantly from 6.4% to 49.7% for single-sensors to 75.9% for multi-sensors. LAI

retrieved from the multi-sensor dataset show good agreement with the field measurements. The correlation coefficient (R^2) is 0.90, and the average root mean square error (RMSE) is 0.42. The network of multiple sensors with 30 m spatial resolution can generate LAI products with reasonable accuracy and meaningful temporal resolution.

Keywords: multi-sensor dataset; the middle reach of the Heihe River Basin; leaf area index; HJ1/CCD; Landsat8/OLI

1. Introduction

Leaf area index (LAI) is defined as half the total foliage area per unit ground surface area [1,2]. It is an important structural parameter in the terrestrial ecosystem and is closely related to the respiration, transpiration and photosynthesis of plants and the net primary productivity [3]. High-precision LAI products with high spatial resolution play an important role in monitoring regional vegetation changes and evaluating the accuracy of low-resolution LAI products [4]. An LAI time series with high spatial resolution is a necessary input for land surface process models and ecological models [5].

Two types of methods can be used to retrieve LAI from remote sensing data: empirical methods and physical model methods [3,6]. Empirical methods, which are based on linear or nonlinear relationship between vegetation indices (VI) and LAI ground observations or simulations of canopy reflectance models, have high computational efficiency [7–10]. However, the empirical relationships are typically dependent on the vegetation types and regions and are generally constructed and used locally [11,12]. In contrast, physical model methods without the regional limitation can be widely applied [9]. Most of the existing 1 km global LAI products are generated from the single-sensor observations based on a single radiative transfer model and on one or two inversion methods [13–18]. However, because of the restriction of observation frequency, obtaining an improvement of the temporal resolution and the accuracy of LAI product turns out to be difficult [19]. Therefore, many studies have explored the possibility of generating LAI products from multiple sensors [11,15,20,21].

The combination of multiple sensor observations can be conducted at the product level and the reflectance level [22]. By minimizing the errors between LAI inversions and field measurements, the product-level combination obtained the LAI value from various LAI products, such as the GLASS LAI product, which combined the MODIS and CYCLOPES LAI products based on a general-regression neural networks (GRNNs) [20,23]. However, the accuracy of product-level combination depends on the accuracy of the generated LAI products [20]. The reflectance-level combination retrieved the LAI from the multi-angular observations, which were obtained by different sensors or satellites [22]. Generally, there are two methods of using the multi-angular observations. The first method matches the bidirectional reflectance distribution function (BRDF) shapes from multi-angular observations with the model simulations, such as the MODIS LAI product (e.g., MCD15A2 and MCD15A3), which is generated based on the MODIS sensor from Terra and Aqua satellites [13]. Another method initially normalizes the multi-angular observations to a nadir-view direction, and then the LAI inversion is achieved from the nadir-view simulation, such as the GLOBCARBON LAI, which is retrieved from the SR/RSR-LAI relationships combining VEGETATION, ATSR-2, AATSR and MERIS multi-sensor

data [11]. Overall, the reflectance-level combination method has great potential to improve the accuracy and temporal resolution of LAI product. However, the limitations of the data preprocessing technologies of multi-sensor influence the applications of the vegetation parameters extracted from the reflectance-level combination dataset.

Currently, the retrieval algorithms and product distributions for the 1 km global LAI products are relatively mature [11,13,14,16–18,20]. The existing LAI products for the 30 m spatial resolution are generally local. However, Ganguly *et al.* is attempting to generate global LAI products using Landsat images [24]. The primary restriction for generating the regional or global LAI products with 30 m spatial resolution is the limited sensor observations during a specific period. For humid and mountainous areas, most of the time, even one cloudless observation from a single sensor cannot be guaranteed during a specific period. Therefore, an effective method to increase the number of observations with 30 m spatial resolution is to use multi-sensor observations. For example, Mousivand *et al.* is producing vegetation state variables (including LAI, fCover and chlorophyll content) using CHRIS, TM and ASTER images over the agricultural test site in Barrax, Spain [21].

Presently, more than 10 international satellites with 30 m resolution sensors are orbiting Earth, such as the Landsat series and SPOT series, as well as CBERS and HJ1 satellite series in China. The revisit period of Landsat8 is 16 days, while that of the SPOT and CBERS satellite series is 26 days. However, the revisit period of the HJ1/CCD satellite series, which combined the two satellites HJ-1A and HJ-1B with CCD1 and CCD2 cameras on each satellite, is increased by up to four days over China. Therefore, this study attempts to develop an algorithm to generate a 30 m resolution LAI product from the HJ1/CCD and Landsat8/OLI dataset from June to August 2013 in the middle reach of the Heihe River Basin, China. The analysis method of the multi-sensor dataset characteristics (e.g., the percentage of valid observations, the distribution of observation angles and the variation between different sensor observations) is introduced in Section 2.1. Considering the differences among the multi-sensor observations after data preprocessing, a data quality control system was designed, and the LAI retrieval workflow is presented in Section 2.2. Section 3 introduces the study area, the experimental data and the data preprocessing for remote sensing images. Section 4 discusses the 10-day LAI products in the study area which were generated from June to August 2013, the spatial integrity and temporal continuity of the LAI products, and the LAI product validation based on field measurements. A summary of the results and conclusions is provided in Section 5.

2. Methodology

2.1. Analysis Method of the Multi-Sensor Dataset Characteristics

The multi-sensor dataset in this study was generated from the HJ1/CCD satellite series, which includes two satellites (HJ-1A and HJ-1B) with two sensors (CCD1 and CCD2) on each satellite, and Landsat8/OLI from June to August 2013 in the middle reach of the Heihe River Basin, China. The LAI retrieval method based on these datasets is closely related to their characteristics. Therefore, before designing the LAI retrieval algorithm, the characteristics of these multi-sensor datasets, including the percentage of valid observations, the distributions of observation angles and the variation between different sensor observations, were analyzed over a 10-day observation period.

At first, considering of the cloud contamination and data gaps, there are invalid observations that do not contribute to the parameter extraction during each 10-day observation period. The percentages of cloudless observations in the total observations were analyzed at certain observation periods. Three typical observation periods, including the period using the data from the maximum of five observations, the minimum of two observations and the average of four observations, were chosen in this study.

Second, in contrast to the multi-sensor dataset with 1 km spatial resolution that have larger scanning widths and observation angles [13,25], the observation angles of the 30 m spatial resolution sensors are substantially smaller due to the scanning widths limitation. The observation angles of Landsat8/ OLI are 0° and those of HJ1/CCD range from 0° to 35°. Because of the overlapped and complemental of the observation angles from different sensors, the distributions of observation angles between the single sensor and multi-sensor were compared in this study.

Finally, considering the differences arising from the sensor band settings, radiation characteristics, pixel locations, and effects of residual clouds and aerosols, the reflectance of multi-sensor even for the same object under similar viewing and illuminating conditions are different. In order to analyse the performance of the reflectance from different sensors after data preprocessing, the reflectance of red and NIR bands from HJ1/CCD and Landsat8/OLI sensors for bare soil, crop and forest were compared under similar viewing and illuminating conditions on the same day (the 186th day). The performance of reflectance between different sensors were evaluated by the R^2, standard deviation (Std), RMSE and homoscedasticity.

2.2. Algorithm of LAI Inversion based on the Multi-Sensor Dataset

2.2.1 Data Quality Control

The primary difference between the multi-sensor and single sensor data was the data consistency. Because of the different performances of the networked satellites, the difference in the satellite observation time and the weather conditions, a discrepancy is possible between the multi-sensor observations at the same or similar observation angles, even after data pre-processing. Therefore, the LAI retrieval algorithm based on the multi-sensor dataset required a data quality control system for selecting the input satellite data.

Two types of data differences occurred in the multi-sensor dataset with 30 m resolution. At first, the reflectance under similar viewing and illuminating conditions from different sensors may be different. Secondly, the reflectance variations under different observation angles may exceed a certain range of values. The questions are emerged: which of the observations are reasonable for the LAI retrieval? How can the abnormal data from these multi-sensor observations be eliminated?

The widely used method for abnormal data elimination, based on the surface object reflectance, is the threshold method, such as the band threshold method and the normalized difference vegetation index (NDVI) threshold method [26–28]. Studies indicated that the instrumental noise and atmospheric correction errors contribute to a Gaussian noise with a standard deviation ranging from 2% to 10%, depending on the surface reflectance bands [26]. Moreover, after the cross-radiometric calibration, the calibration accuracy of four spectral bands of HJ1/CCD sensor was 5% [29]. Therefore, for the same

object at similar observation angles, the errors caused by the data preprocessing were defined as 15% of reflectance.

In another case, a threshold was typically used to control the reasonable reflectance difference by the BRDF effects. During the 16-day period of the MODIS product, if the band reflectance had a coefficient of variation exceeding a fixed threshold (e.g., 0.3), then the observation with the greatest absolute reflectance difference (compared with the mean reflectance of the observations in the 16-day period) was considered an outlier [28]. Moreover, Leblanc *et al.* noted that the NDVI difference due to the different observation angles for forest types may be larger than 0.2 [30]. Additionally, Walter *et al.* demonstrated that the difference between the maximum and minimum NDVI can reach 0.3 due to angle effects when the LAI is less than 2 [31]. Therefore, the NDVI difference of multi-angular data generated from the multi-sensor network observations should be less than 0.3. Any NDVI difference that was greater than 0.3 was considered noise.

In this study, the following thresholds were set to control the data difference:

(1) When the NDVI difference for all of the observations in a period was greater than 0.3, the observation with the lower NDVI will be eliminated.

(2) When the reflectance difference at the same or similar observation angles was greater than 15% of reflectance, the observation with the lower NDVI will be eliminated.

2.2.2. LAI Retrieval Method

Research indicates that the estimations of daily canopy photosynthesis can differ by 20% for black spruce when clumping is considered [32]. However, the existing canopy reflectance models, such as the SAIL model [14] and 3D radiative transfer model [13], do not consider the foliage clumping effects on canopy simulations. Therefore, Yan *et al.* introduced the Nilson parameter, which describes spatial foliage clumping, into a unified model [33]. Based on the idea of the geometric optical model, the unified model calculated four components (the visibly illuminated and shadowed leaves and the visibly illuminated and shadowed ground) based on the leaf scale and simulated different vegetation types, such as forest, grass and crops, with different input parameters [33]. Considering the obvious clumping effects in high-resolution remote sensing images, the unified model was selected for the LAI inversion in this study.

The unified model, which is a nonlinear model with many input parameters, cannot directly identify the LAI inversion values. The look-up table method is a superior and faster tool for simulating the various relationships between input parameters and canopy reflectance before parameter retrieval. Therefore, a look-up table was established from the simulation of canopy reflectance in the green, red and NIR bands of HJ1/CCD and Landsat8/OLI under different observation conditions based on the unified model. Then, the LAI was retrieved from single sensor data based on the look-up table [34,35].

The input data for LAI retrieved from a multi-sensor dataset with a 30 m resolution included a land-use map and multi-sensor images over a 10-day period. Although the number of valid observations of the multi-angular dataset constructed from HJ1/CCD and Landsat8/OLI was higher than that from single sensor data, the observation angles might overlap, providing redundant information. Therefore, only the valid observations that meet the data accuracy requirements were used to LAI retrieval. Then, considering the reflectance difference among various observation angles and different sensors, the synthetic LAI values were averaged the LAI retrievals from single sensor data during each 10-day

observation period to decrease the LAI inversion variations. The flowchart of LAI retrieval algorithm based on the 30 m resolution multi-sensor dataset is shown in Figure 1.

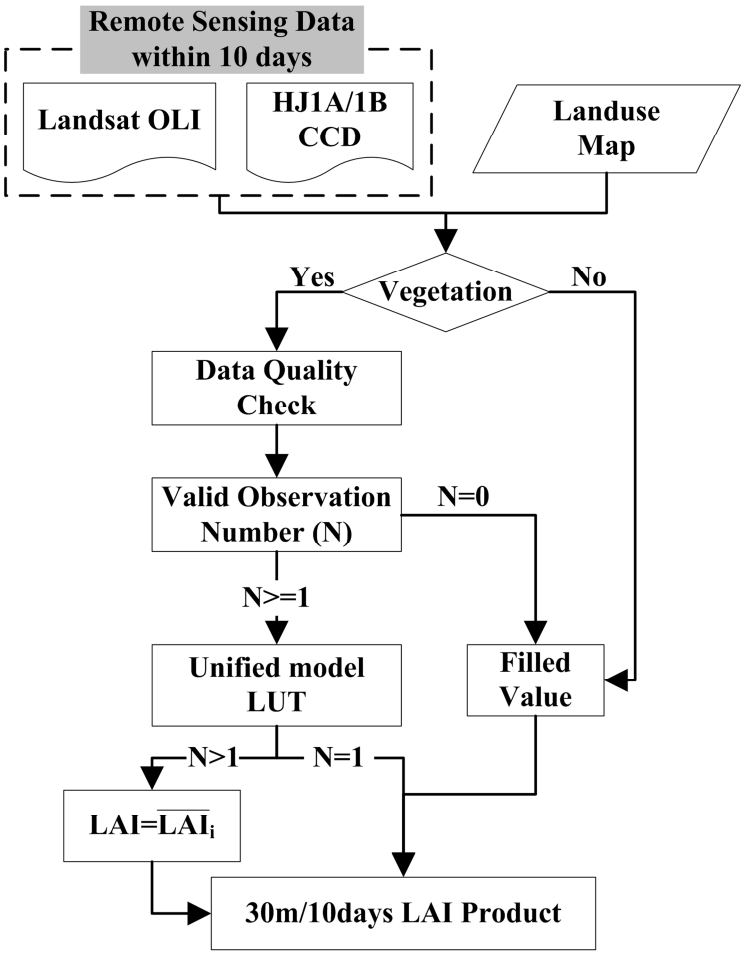

Figure 1. Flowchart of the LAI retrieval algorithm from the 30 m resolution multi-sensor dataset.

3. Study Area and Data

3.1. Study Area

The Heihe River Basin is located in the middle of the Hexi Corridor, Gansu Province, China (97°20′E–102°12′E, 37°28′N–39°57′N). The observation programs, WATER (Watershed Allied Telemetry Experimental Research) and HiWater (Heihe Watershed Allied Telemetry Experimental Research) were performed from 2008 to 2013 [36–38]. The middle reach of the Heihe River Basin, which is a well-known agricultural area, is selected as the study area (99°24′8″E–100°48′20″E, 38°30′20″N–39°35′59″N) (Figure 2). Corn is the dominant crop in this area (Figure 2a).

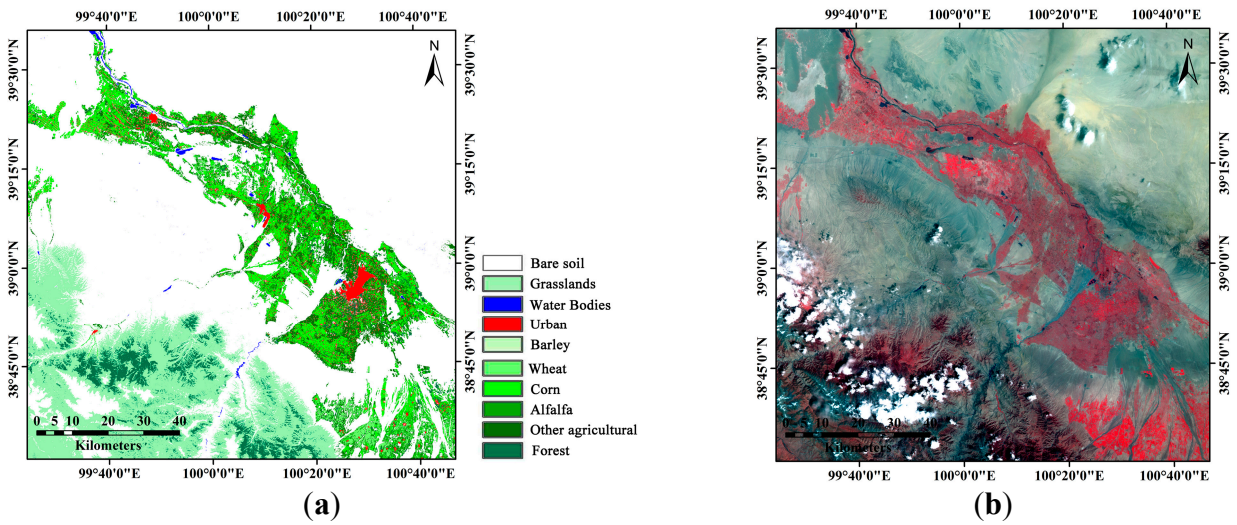

Figure 2. (**a**) Land cover map of the study area in the middle reach of the Heihe River Basin in July 2013. The major vegetation types are corn (green), grassland (light green), forest (dark green) and urban lands (red). (**b**) False color composite of HJ1/CCD image for the study area on 3 June 2013.

3.2. Satellite Data

The satellite sensors used to construct the multi-sensor dataset in this study include HJ1/CCD and Landsat8/OLI, launched on 11 February 2013. The available multi-sensor dataset were obtained after February 2013. Landsat8/OLI data were downloaded from the USGS website [39], and HJ1/CCD data were downloaded from the China Centre for Resources Satellite Data and Application website [40]. The primary sensor characteristics of HJ1/CCD and Landsat8/OLI are shown in Table 1. These two sensors have similar spectral characteristics and spatial resolutions; however, the HJ1/CCD data has a broader swath width and a shorter revisit time.

Table 1. Comparison of the sensor band settings and characteristics between HJ1/CCD and Landsat8/OLI.

Sensor	**HJ1/CCD**		**Landsat8/OLI**	
	Band	Spectral range (μm)	Band	Spectral range (μm)
Spectral characteristics	1	0.43–0.52	2	0.45–0.515
	2	0.52–0.60	3	0.525–0.60
	3	0.63–0.69	4	0.63–0.68
	4	0.76–0.90	5	0.845–0.885
Spatial resolution (m)	30		30	
Swath width (km)	360 (single), 700 (two)		170 × 185	
Revisit time (days)	4		16	

Data preprocessing included the cross-radiometric calibration, the geometric correction and the atmospheric correction, which were implemented by a quantitative remote-sensing production system for the multi-sensor dataset [41]. The cross-radiometric calibration of HJ1/CCD data was conducted by a method that considers the characteristics of surface BRDF [42]. The calibration accuracy of the four

spectral bands of HJ1/CCD sensor was 5%, which meets the requirements of absolute radiometric calibration accuracy [29]. Using the global TM mosaic image as a reference, the geometric correction method was used based on the hierarchical registration method, and the RMSE was less than 2 pixels for hilly and flat terrains [43]. The atmospheric correction was conducted using a space-based aerosol optical depth (AOD) retrieval algorithm, which was proposed by Zhong [44]. The difference between the AERONET measurements and the AOD retrieved from HJ1/CCD data range from –0.14 to 0.31, approximately 50% of the derived AOD values correlate with AERONET AOD with low discrepancy (less than 0.15), and the RMSE for Xianghe and Beijing is 0.18 and 0.21, respectively [45]. The reflectances of the four spectral bands of the HJ1/CCD sensor after atmospheric correction meet the requirements for application. The reflectance and angle information dataset from the multiple sensors was obtained for the middle reach of the Heihe River Basin from June to August 2013.

3.3. LAI Field Measurements

LAI field measurements used in the analysis and validation were acquired by the wireless sensor network (WSN) and the LAI-2200 optical instrument from 11 June to 29 August 2012. Prior to validation of the LAI products, a land cover map and the historical multi-temporal VI products were used as *a priori* knowledge to describe the vegetation spatial distribution and growing characteristics at the validation sites during the observation periods (Figures 3 and 4). The sampling sites with minor inter-annual changes during vegetation growth stages and more reasonable characteristics according to the vegetation phenology can be used to parameters validation [46,47]. Figure 3 shows that some of the planting area for corn crops in July 2012 were used for other crops in July 2013. Therefore, LAI field measurements, which were both located in the corn planting area in July 2012 and 2013, were used for validation. Using the MODIS NDVI products (e.g., MOD13A1 and MYD13A1) with a 500 m spatial resolution, the temporal profiles of the mean NDVI for all of the selected LAI sample plots in the study area from the 185th to the 241st day of 2012 and 2013 were similar (Figure 4a). However, there were only six corn sample plots measured with the nearest positions at the periods of 11 to 18 June and 4 to 10 July both in the year of 2012 and 2013 (Figure 4b). The difference of LAI measurements between two observation periods were much lower between the year of 2012 and 2013 (R^2 is 0.98 and RMSE is 0.15). The maximum relative error (defined as the absolute error of LAI field measurements between 2012 and 2013 divided by LAI field measurements in 2012) was 16.08%, the minimum value was 0.98%, and the average value was 6.72%. Therefore, LAI field measurements obtained in 2012 could be used to validate the LAI inversions in 2013.

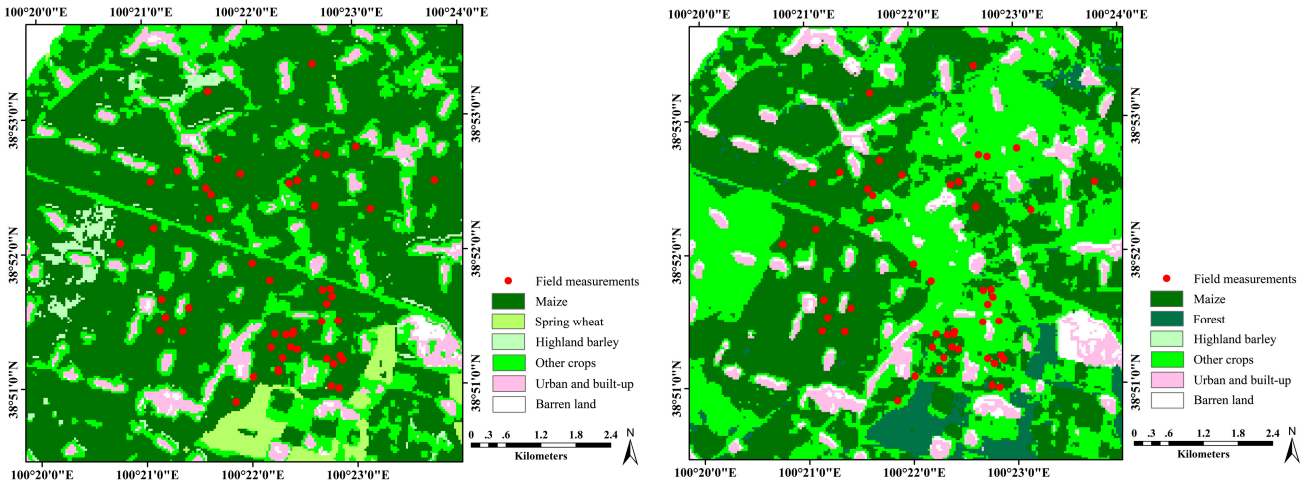

(**a**) (**b**)

Figure 3. Land cover maps and the LAI field measurements of the study area in July 2012 (**a**) and July 2013 (**b**). The red point is the LAI field measurement, the green area is covered by corn crops, and the light green area is covered by other crops.

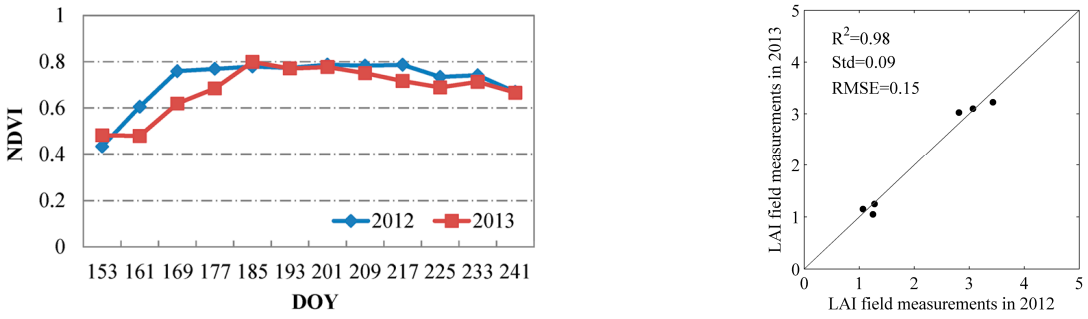

(**a**) (**b**)

Figure 4. (**a**) Temporal profiles of mean MODIS NDVI for all of the selected LAI sample plots in the study area from the 153rd to the 241st day of 2012 (blue line) and 2013 (red line). (**b**) Comparison of the six corn sample measurements with similar observation times in 2012 and 2013.

In 2012, a WSN system, which was designed by Y. Qu [48], was used to automatically measure the LAI values in the HiWater experiment. LAI was calculated from the transmitted radiance observations from 5 viewing angles based on the Beer-Lambert law [48]. The 19 points measured by the WSN in a 3 km × 3 km cropland area and 11 points measured by the LAI-2200 optical instrument near the corn sample fields from 11 June to 29 August 2012 were selected for LAI validation. The WSN was designed to automatically measure LAI every day, and LAI in the corn fields were measured by LAI-2200, with measurements from six to 18 days. All of the selected LAI field measurements were averaged over 10-day intervals according to the synthetic product period. The observation period was marked as the first day of the 10-day interval, for example, the period from 1 June to 10 June 2012 was recorded as 1 June 2012. A portion of the selected field measurements is shown in Table 2, the selected sites that are missing more than four field measurements during the observation times are not shown here, but have used to LAI validation. In addition, other LAI field measurements were

obtained at the period of 11 to 18 June and 4 to 10 July 2013 (Table 3). LAI field measurements of these two experiments were obtained by the LAI-2200 optical instrument. To avoid measurement errors caused by direct sunlight, the measurements were obtained from 06:30–10:00 and from 16:30–19:30, and the LAI value at each site was measured twice.

Table 2. Description of portions of the selected observation sites by WSN and LAI-2200 for LAI inversion validation obtained from 11 June to 29 August 2012. The "--" indicates "no observation data".

Lat (°)	Lon (°)	LAI Measurements in 2012							
		11th Jun.	21st Jun.	1st Jul.	11th Jul.	21st Jul.	31st Jul.	10th Aug.	20th Aug.
100°21′11.16″E	38°51′31.28″N	--	1.97	3.14	3.09	3.03	3.33	2.69	3.00
100°21′37.08″E	38°52′14.92″N	1.01	2.58	--	3.82	--	2.91	2.71	--
100°21′55.08″E	38°52′34.79″N	1.14	--	3.33	3.31	3.52	3.02	--	3.14
100°21′03.96″E	38°52′31.80″N	1.13	--	--	3.89	3.73	3.51	4.07	3.09
100°21′37.08″E	38°53′11.69″N	0.94	2.79	3.76	3.50	--	3.64	--	--
100°22′36.84″E	38°53′23.32″N	1.12	--	3.44	--	4.13	3.28	--	3.02
100°23′45.60″E	38°52′30.68″N	1.41	2.21	3.47	2.87	3.27	2.99	2.41	3.20
100°22′22.44″E	38°51′16.99″N	0.87	1.93	3.45	--	3.33	3.86	3.42	2.53
100°21′50.76″E	38°50′53.09″N	1.14	2.92	--	3.03	3.38	--	--	3.23
100°22′11.28″E	38°51′16.96″N	--	--	2.82	3.42	3.83	3.79	3.45	2.65
100°21′24.48″E	38°51′35.39″N	--	2.98	--	3.06	3.35	3.05	3.33	3.30
100°22′46.56″E	38°51′09.25″N	--	--	--	2.99	2.94	2.59	2.64	1.89

Table 3. Description of LAI field measurements obtained from 11 to 18 June and to 10 July 2013.

Lat.	Lon.	LAI Measured on 11th–18th June 2013	Lat.	Lon.	LAI Measured on 4th–10th July 2013
100°23′09.96″E	38°52′56.99″N	0.96	100°22′16.32″E	38°51′16.34″N	3.39
100°22′38.28″E	38°52′11.21″N	1.17	100°22′49.80″E	38°51′28.12″N	2.78
100°21′24.48″E	38°52′20.32″N	1.37	100°22′37.56″E	38°51′28.40″N	2.35
100°21′35.28″E	38°52′27.80″N	1.60	100°21′41.40″E	38°52′41.12″N	3.87
100°21′45.00″E	38°52′38.10″N	1.53	100°21′20.52″E	38°52′36.16″N	3.56
100°20′57.48″E	38°52′54.52″N	1.70	100°21′38.16″E	38°52′25.54″N	3.07
100°20′55.32″E	38°52′23.59″N	1.92	100°21′05.04″E	38°52′11.21″N	3.16
100°21′54.72″E	38°53′06.20″N	1.91	100°24′43.20″E	38°51′16.09″N	3.08
100°23′02.76″E	38°52′07.40″N	1.13	100°22′30.36″E	38°45′30.64″N	3.24
100°23′13.92″E	38°52′37.99″N	1.06	100°23′11.40″E	38°47′40.63″N	4.50
100°22′16.32″E	38°52′36.98″N	1.66	100°22′41.88″E	38°47′47.62″N	4.12
100°22′04.80″E	38°51′30.40″N	1.24	100°24′05.04″E	38°48′50.80″N	2.31
100°22′55.20″E	38°51′39.89″N	1.16			
100°20′57.84″E	38°51′47.81″N	1.28			
100°21′45.72″E	38°51′46.01″N	1.41			
100°22′15.60″E	38°51′46.40″N	1.89			
100°20′52.08″E	38°20′02.05″N	1.10			

4. Results and Discussion

4.1. Analysis Results of the Multi-Sensor Dataset Characteristics

4.1.1. Percentage of Valid Observations

Based on the multi-sensor dataset, the frequency of all the observations are shown in Figure 5. Due to the short revisit period, HJ1/CCD was the primary data source for the multi-sensor observations, accounting for 76% of the entire dataset. The Landsat8/OLI data only accounted for 24% of the total. Generally, there are at least three observations available over a 10-day period. Occasionally, there are two or fewer observations, such as for the period beginning 11 June 2013.

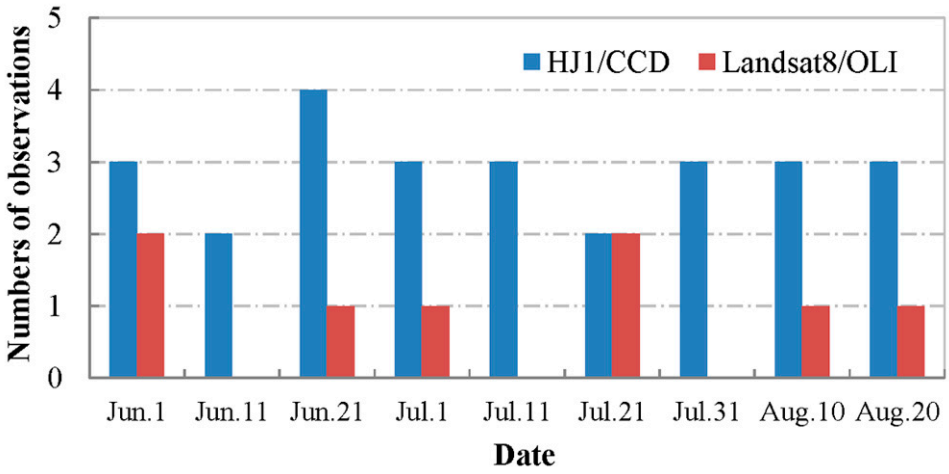

Figure 5. Statistical distributions of the multi-sensor observations in a 10-day period.

Considering the invalid observations due to the cloud contamination and data gaps, the percentages of cloudless observations in the total observations over three typical observation periods (including the period with data from the maximum of five observations, the minimum of two observations and the average of four observations) were shown in Figure 6. The number of valid observations ranges from 1 to 5, and 0 represents the absence of a valid observation. First, five satellite sensors (three HJ1/CCD and two Landsat8/OLI images) were available during the period of 1 June 2013, and most of the pixels have four or five valid observations in this period due to the favorable weather conditions (Figure 6a). Second, only two sensor observations from HJ1/CCD were available in the period of 11 June 2013. In some areas, there are no observations available, and in other areas, a maximum of two observations were available (Figure 6b). During the period of 10 August 2013, four satellite images were available. The distribution of valid observations was close to a normal distribution which was primarily because of the partial cloud cover in the area, and the maximum of two observations were available (Figure 6c). On the whole, during each 10-day observation period, the valid observations increase from an average of one based on single sensor to an average of over three based on multiple sensors. The network of multiple sensors significantly improves the feasibility of 30 m remote sensing LAI products and their temporal resolution.

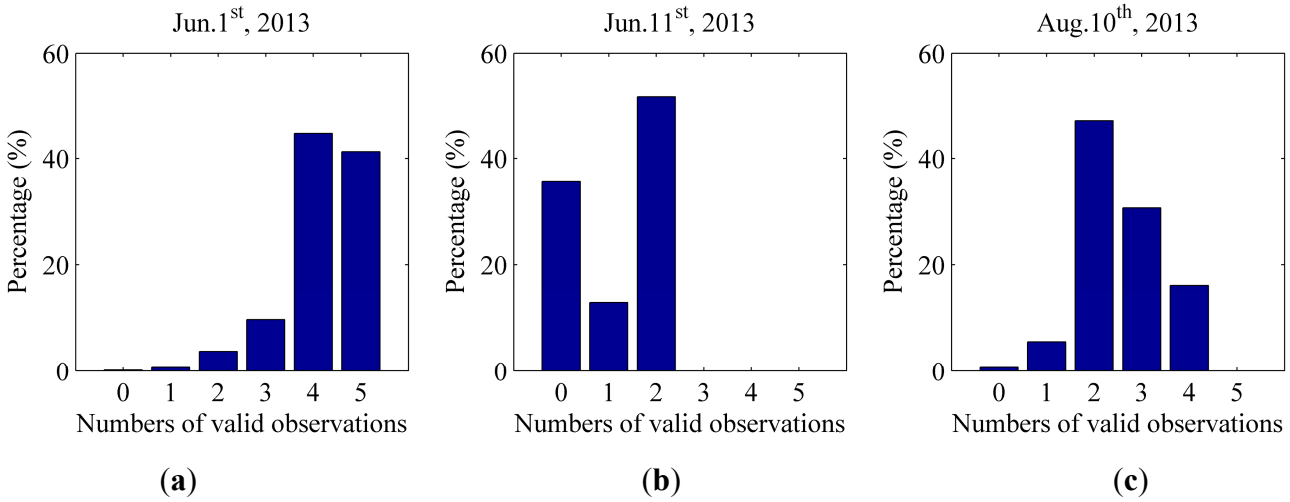

Figure 6. Statistical distributions of valid observations during three special observation periods: (**a**) 1 June 2013; (**b**) 11 June 2013; and (**c**) 10 August 2013.

4.1.2. Distribution of Observation Angles

Except for the period of 11 June 2013, in which only two sensors were available, the observation angles distributions of the multi-sensor dataset were analyzed over each observation period. The observation angles of each image were classified from 0° to 35° with an interval of 5°. Considering the nadir observation of Landsat8/OLI, the statistical analysis of the nadir angle was conducted separately. Figure 7 presents three typical distributions of observation angles between the single sensor and the multi-sensor. The distributions of observation angles from the single sensor were more clumped, but the distributions of observation angles from the multi-sensor dataset were much wider. During the period of 1 June 2013, the observation angles of three HJ1/CCD images and two Landsat8/OLI images were concentrated from 0° to 15° (Figure 7a). In Figure 7b,c, the observation angles were distributed from 0° to 35° with different distribution patterns. The observation angles from different sensors can complement each other, but they can also overlap. The observation angles increased randomly in different period to form different distribution patterns. Overall, the observation angles of the multi-sensor dataset for all of the pixels were statistically enriched compared with the single sensor. However, for an arbitrary pixel, the observation angles enrichments for the multi-sensor data with 30 m resolution were limited, and the information from the increasing angles was also limited.

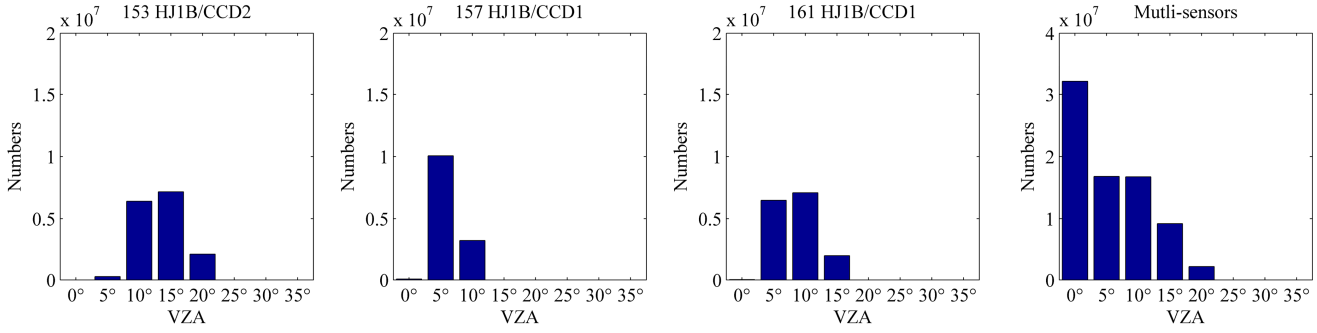

Figure 7. *Cont.*

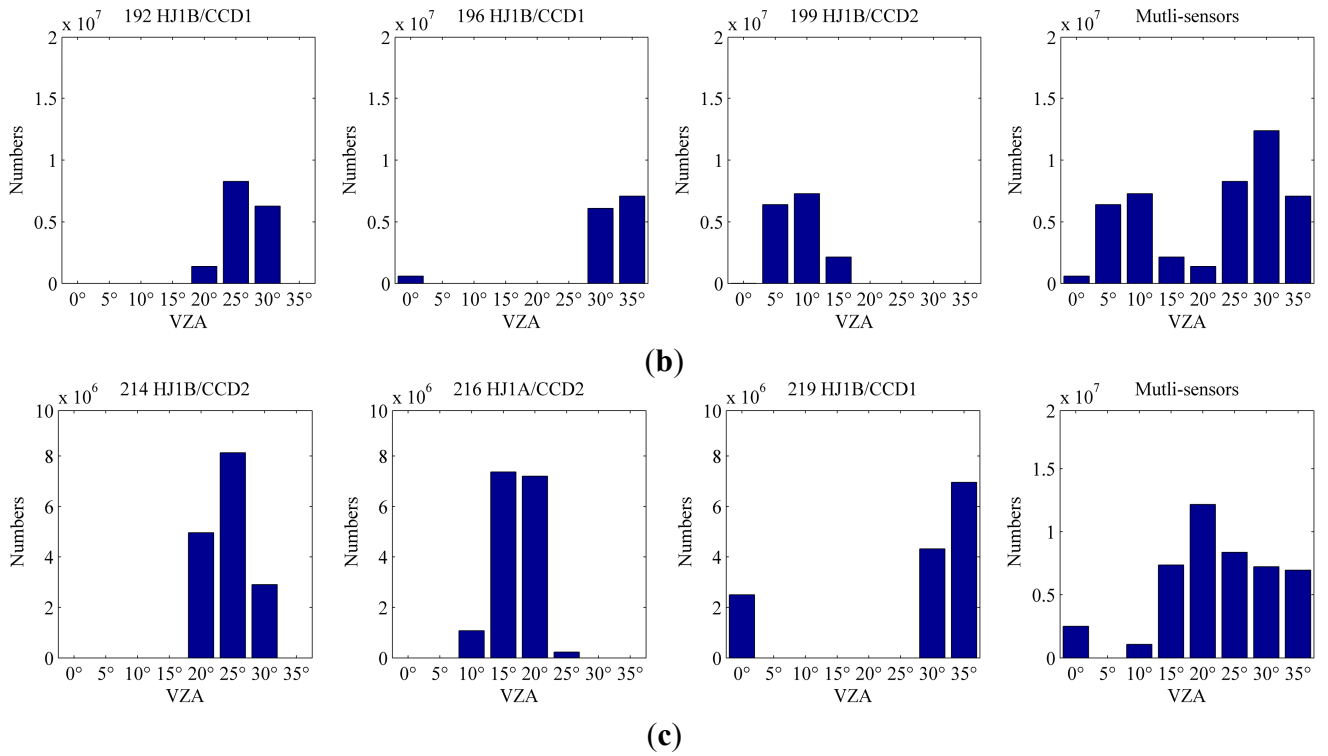

Figure 7. Distributions of the observation angles for three typical observation periods. (**a**) 1 June 2013; (**b**) 11 July 2013; and (**c**) 31 July 2013.

4.1.3. Variation between Different Sensor Observations

The percentage density plot of reflectance between HJ1/CCD and Landsat8/OLI in the red and NIR bands for bare soil, crop and forest under similar viewing and illuminating conditions on the 186th day is shown in Figure 8. The performance of the reflectance between two sensors were evaluated by the R^2, standard deviation (Std), RMSE and homoscedasticity (Table 4). For bare soil, most of the pixels were clumped with high density both in red and NIR band (Figure 8a). The reflectance of HJ1/CCD in the red and NIR bands agreed better with Landsat8/OLI, which the R^2 was 0.88 and 0.89 and the RMSE was 0.013 and 0.012 for the two bands, respectively (Table 4). For crop type, the reflectance of HJ1/CCD in the red and NIR bands slightly deviated with Landsat8/OLI, especially in the red band (Figure 8b). The R^2 value of these two bands was 0.79 and 0.86, and the RMSE was 0.036 and 0.023, respectively (Table 4). For forest type, the reflectance in the red and NIR bands was more dispersed with Landsat8/OLI, particularly in the red band (Figure 8c). The R^2 value of these two bands was 0.5 and 0.59, while the RMSE was 0.027 and 0.055, respectively (Table 4). However, the variances for all of the pixels were not pass through the hypothesis at a 0.05 confidence level (Table 4). The reflectance variances in red and NIR band between HJ1/CCD and Landsat8/OLI were more comparable for bare soil types and varied for forest and crop types.

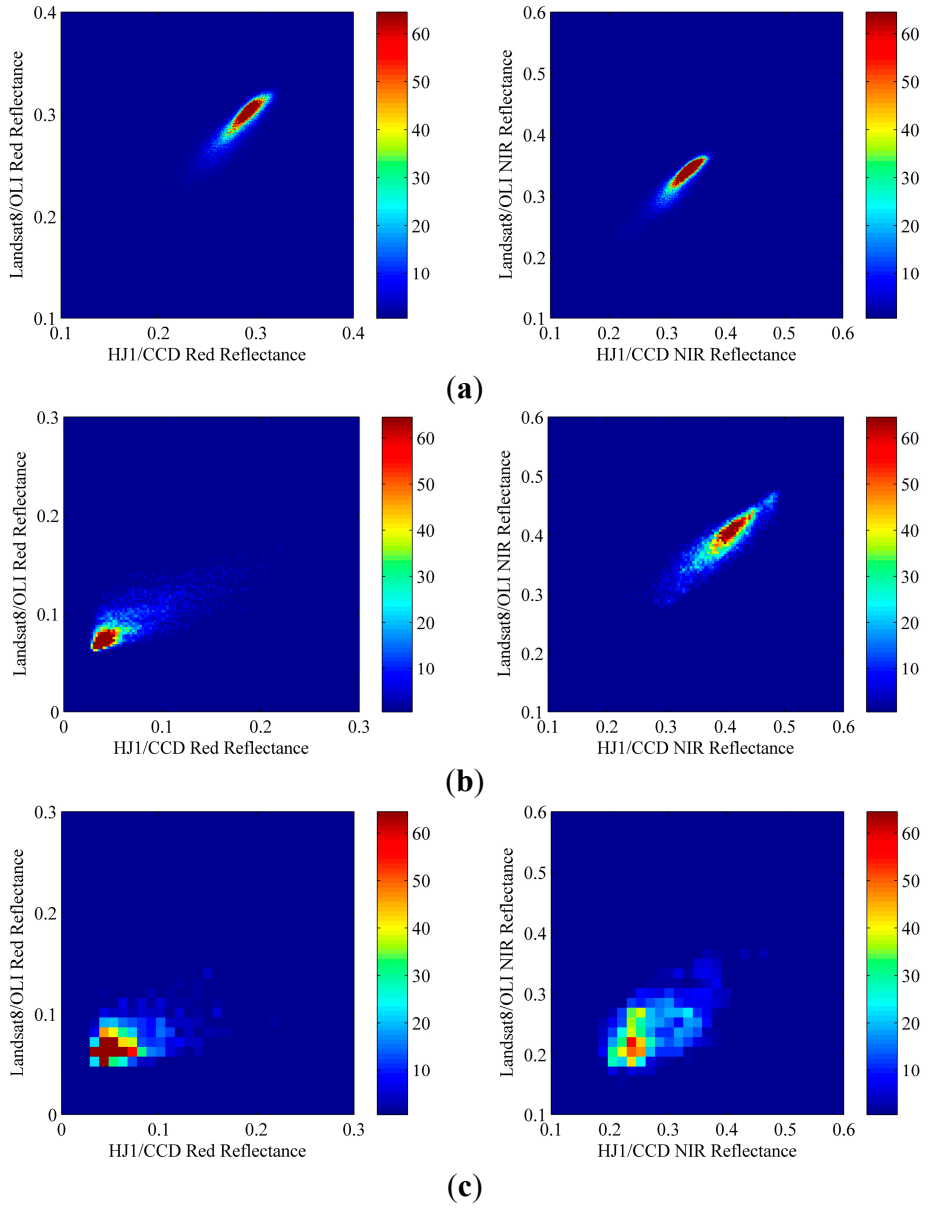

Figure 8. Density scatter plot of the reflectance in red and NIR bands between the HJ1/CCD and Landsat8/OLI dataset for bare soil (**a**), crop (**b**) and forest (**c**) on the 186th day.

Table 4. Statistics of the performance of reflectance comparison both in red and NIR band between the HJ1/CCD and Landsat8/OLI dataset. (* The confidence interval presents the true ratio of population variance, and the confidence level is 0.05.)

Types	Bands	Samples	R^2	RMSE	Std.	Confidence Interval *	Homoscedasticity
Bare soil	Red	120,700	0.88	0.01	0.01	94%–96%	No
	NIR	120,700	0.89	0.01	0.01	88%–91%	No
Crop	Red	14,550	0.79	0.04	0.02	33%–35%	No
	NIR	14,534	0.86	0.02	0.02	66%–70%	No
Forest	Red	1529	0.50	0.03	0.02	26%–32%	No
	NIR	1518	0.59	0.06	0.03	55%–67%	No

To clarify the sensor observation difference in the LAI inversion for each pixel, the reflectance difference from the multi-sensor dataset was analyzed. The reflectance of multi-sensor observations for a random crop and forest pixels between 21 June and 30 June is shown in Figure 9. Because of the close satellite observation time, the SZA of the crop pixel was 23.22°–29.88° (Figure 9a), and the SZA of the forest pixel was 23.22°–29.35° (Figure 9b). The maximum difference of SZA was approximately 6.6°. With the similar SZA and VZA, the reflectances of the same object from different sensors were different. For the crop pixel in Figure 9a, when VZA was close to 0°, the reflectance in the red and NIR bands ranged from 0.07 to 0.12 and from 0.33 to 0.35, respectively. When VZA was close to 9°, the reflectances in the red band for the two sensors were approximately 0.08, and the reflectances in the NIR band ranged from 0.33 to 0.38. For the forest pixel in Figure 9b, when VZA was close to 5°, the reflectances in the red and NIR bands ranged from 0.07 to 0.08 and from 0.33 to 0.39, respectively. Based on this analysis, the maximum reflectance difference was 0.05 for the red band and 0.06 for the NIR band under similar SZA.

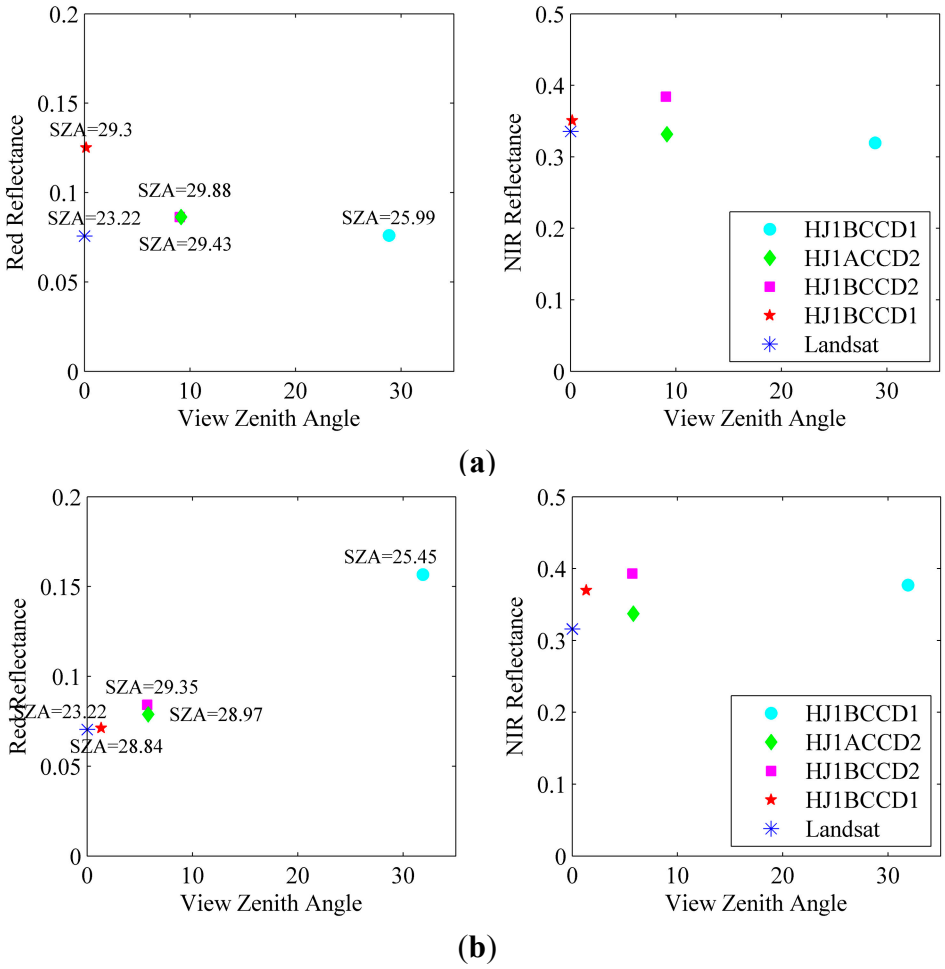

Figure 9. Variation between different sensor observations for crops (**a**) and forests (**b**) from 21 to 30 June 2013.

This analysis implies that the complementarity of the observation angles and the multiple sensors with a 30 m spatial resolution is poorer than that of the multiple sensors with a 1 km spatial resolution. The multiple sensors provide limited observation angles for each pixel, and the observation angles of

different sensors occasionally overlap, which makes it impossible to outline the BRDF curve for all of the pixels through the multi-sensor dataset. The observation angles with a more dispersive distribution are helpful for parameter extraction. Similar observation angles that have a strong correlation may contain more redundant information, which would reduce the inversion rate and hinder the information gain in the parameter extraction [25]. Therefore, for the networking of 30 m spatial resolution sensor data in this study, the improvement of LAI inversion is more dependent on the availability of high-quality observations than on the increase of observation angles.

4.2. LAI Inversion Results and Validation

The 10-day LAI products with a 30 m spatial resolution in study area were generated from the multi-sensor dataset constructed by HJ1/CCD and Landsat8/OLI from June to August 2013. LAI was retrieved from a look-up table based on the unified model and land cover map. The Gobi Desert, bare lands and water bodies were not involved in this method, and the LAI values of these types were filled in with an invalid value. Figure 10 shows three LAI maps on 1 June, 11 July and 20 August 2013. For the forest type, some pixels missed the LAI inversions due to heavy cloud coverage.

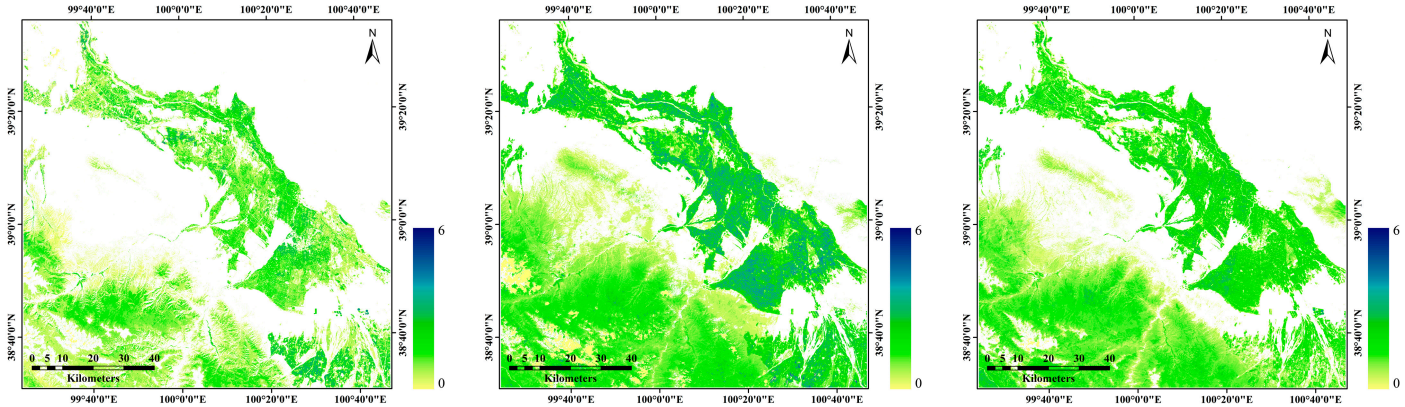

Figure 10. Maps of LAI inversion over three 10-day observation periods from HJ1/CCD and Landsat8/OLI. (**a**) 1 June 2013; (**b**) 11 July 2013; and (**c**) 20 August 2013.

4.2.1. Improvement of the Valid LAI Inversion from the Multi-Sensor Dataset

For single-sensor data, the pixels that failed to retrieve the LAI may be contaminated by clouds, missed by data gaps, or had poor data preprocessing accuracy. The percentage of valid LAI inversions from single-sensor data is typically limited. However, due to the observation complementation from different sensors, the pixels that failed to retrieve LAI from single-sensor data would be replaced by high-quality data from other sensors. Therefore, the percentage of valid LAI inversion from multi-sensor data would be significantly improved compared with that from a single-sensor. The percentages of valid LAI inversions to total inversions from single-sensor data and multi-sensor data during the period of 1 June 2013, which has the maximum of five observations, were analyzed in Figure 11. Because of heavy cloud cover, the percentages of valid LAI inversions from single images of HJ1B/CCD2 on the 153rd day and Landsat8/OLI on the 154th day were only 6.4% and 24.6%, respectively. The single HJ1B/CCD1 image on the 157th day had the largest proportion of valid LAI inversions

(49.7%). On the 161st day, the proportions of valid LAI inversions from the single HJ1B/CCD1 and Landsat8/OLI images were 46.5% and 38.9%, respectively. The proportion of valid LAI inversions retrieved from multi-sensor dataset significantly increased to 75.9%. In summary, the spatial coverages of the LAI product based on the multi-sensor dataset can be significantly improved.

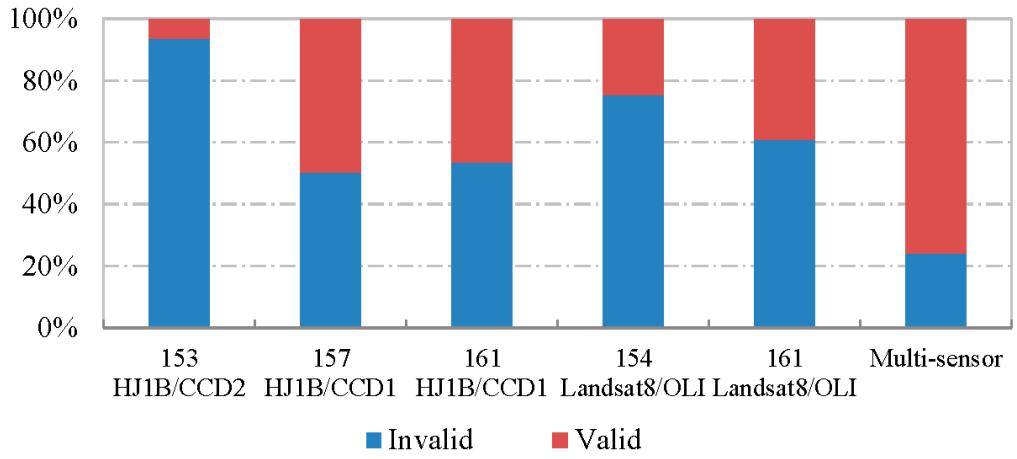

Figure 11. Distribution of valid LAI inversions during the period of 1 to 10 June 2013.

4.2.2. Validation

The primary advantage of multi-sensor networking is to increase the observation frequency, which significantly improves the feasibility of generating 30 m remote sensing LAI products and their temporal resolution. All of the selected LAI field measurements acquired from 2012 and 2013 were used to LAI validation (Figure 12), and portions of the LAI multi-temporal measurements were used to analyze the temporal continuity of LAI inversions (Figure 13).

LAI retrieved both from single sensor data (Figure 12a,b) and from the combining HJ1/CCD and Landsat8/OLI dataset (Figure 12c). The performances of LAI retrieved from HJ1/CCD data and Landsat8/OLI data were not well (Figure 12a,b). The relationships between LAI inversions and the field measurements had larger Std (0.57 and 0.49) and RMSE (1.01 and 0.74) but lower R^2 (0.75 and 0.40), respectively. Some of LAI inversions from single sensor data, which contaminated by cloud or with poorly accuracy of data processing, should be eliminated. Therefore, LAI retrieved from the combining HJ1/CCD and Landsat8/OLI dataset showed better agreement with the field measurements (Figure 12c), with an R^2 of 0.90, a Std. of 0.24 and an RMSE of 0.42. The maximum relative error (defined as the LAI absolute error divided by the true value) from all of the LAI field measurements is 51.74%, the minimum relative error is 0.03%, and the average relative error is 12.94%.

Based on the LAI multi-temporal measurements displayed in Table 2, the validation results with 12 WSN and LAI-2200 sample plots from 11 June to 29 August 2013 for corn were compared in Figure 13. Except for the point of 8, 9 and 11, the RMSE of the other plots was lower than 0.5. The temporal profiles of the LAI inversion were relatively smooth and better coincide with the field measurements. The network of multi-sensor with 30 m spatial resolution can generate LAI products with reasonable accuracy and meaningful temporal resolutions.

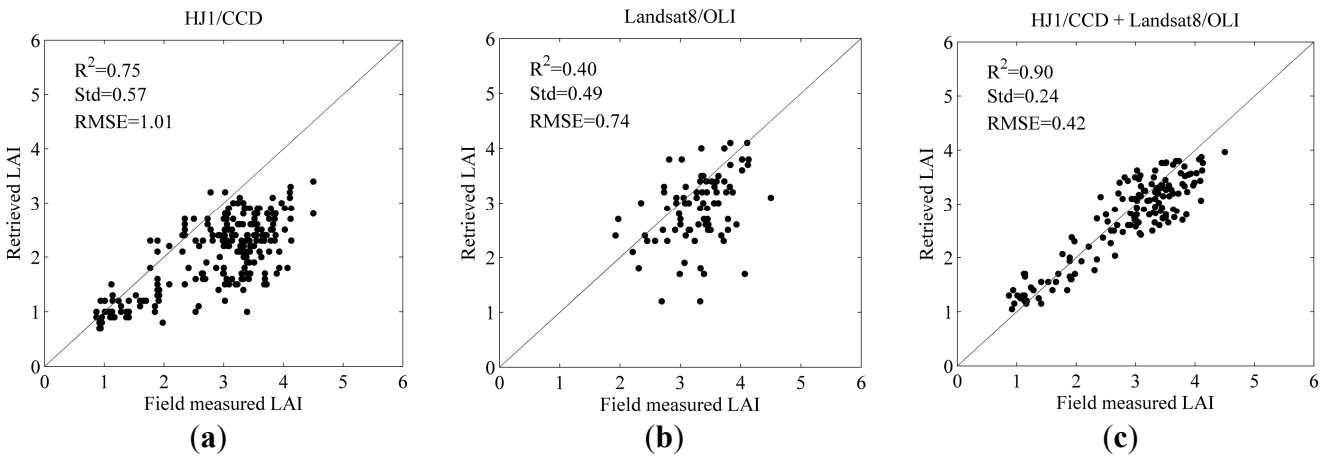

Figure 12. Comparison of the LAI inversions with the field measurements by WSN and LAI-2200 for crops from July to August 2013. (**a**) LAI inversions of HJ1/CCD data; (**b**) LAI inversions of Landsat8/OLI data; (**c**) LAI inversions of the combining HJ1/CCD and Landsat8/OLI dataset.

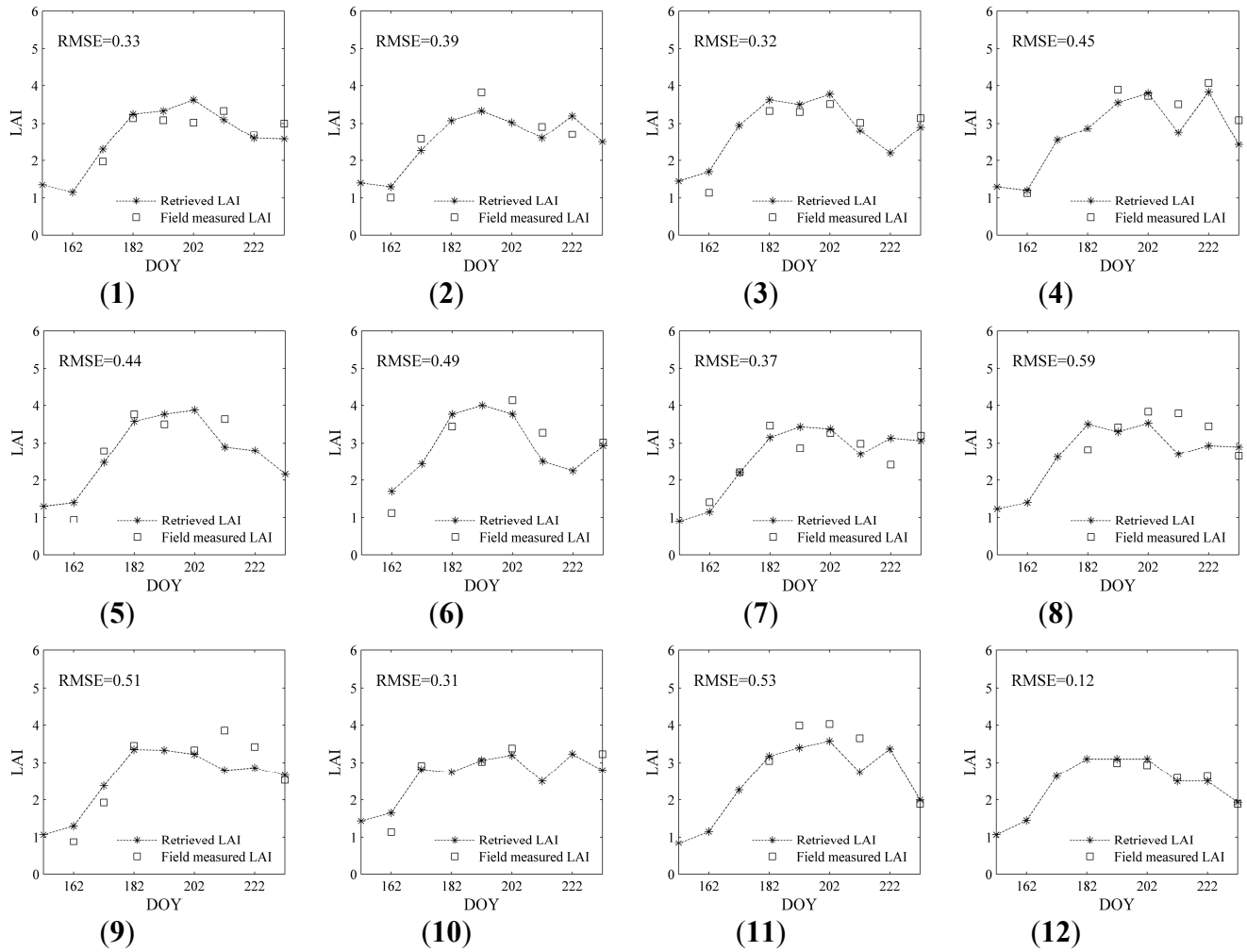

Figure 13. Comparison of the LAI multi-temporal inversion with 12 field measurements (**1**–**12**) by the WSN and LAI-2200 for corn.

4.2.3. Comparison of LAI Inversions with Existing Studies

Considering the uncertainties from data preprocessing and LAI retrieval process, the variations of LAI inversions from different satellite sensors in each observation period were analyzed. More than 45% of the whole pixels showed a maximal difference less than 0.5, and more than 30% range from 0.5 to 1. Moreover, the variations between LAI inversions from different satellite sensors and the LAI field measurements in each observation period was also analyzed. More than 25% of the whole field measurements showed a maximal difference less than 0.5, more than 50% range from 0.5 to 1, and about 25% greater than 1. However, the data quality control in the algorithm can remove some inconsistent observations; thus, the inconsistent observations under different observation angles cannot be identified once they are removed. These inconsistencies can still influence the inversion accuracy, causing the large variation of LAI retrievals from pixels of different sensors.

LAI inversions of this study were also compared with the existing studies. The LAI inversions from eight Landsat images mainly in 2005 was compared with MODIS LAI product (MOD15A2) [15,24]. The maximum LAI differences between Landsat-derived LAI and MODIS LAI product are within 0.2 absolute units of LAI over grasses, crops, and evergreen needle-leaf forests (ENF), within 0.5 absolute units for savannas, within 0.6 absolute units for evergreen broadleaf forests (EBF), within 2 absolute units for deciduous needle-leaf forests (DNF), within 0.6 LAI absolute units in the lower LAI values from 2 to 3 and within 1.3 absolute units in the higher LAI region from 4 to 6 for deciduous broadleaf forests (DBF) [24]. The MODIS LAI values are overestimated by about 12% (RMSE = 0.66) than field measurements when all biomes are taken into consideration [15]. In addition, the accuracy of LAI retrieved from multi-temporal and multi-sensor dataset with 30 m spatial resolution were 0.75 on 19 June 2008, 0.69 on 20 June 2008, 0.72 on 21 June 2009 and 0.70 on 22 June 2009 for the agricultural test site in Barrax, Spain [21]. The RMSE of LAI inversions from multi-sensor dataset in this study with field measurements was 0.42, and the accuracy of the LAI inversion was convincing.

Moreover, LAI inversions from the PROBA/CHRIS and Hyperion remote sensing data based on the unified model look-up table were compared with LAI inversions of this study in the middle reach of the Heihe River Basin, China [34,35]. The RMSE of LAI inversions based on the PROBA/CHRIS data on 4 June 2008 over 11 field measurements was 0.08 [34] , while the RMSE of LAI inversions based on the Hyperion data on 15 July 2008 over 18 field measurements was 0.11 [35]. LAI retrieved from the look-up tables based on the unified model can estimate LAI accurately through analyzing the canopy anisotropy and effectively removed the effect of background. However, the RMSE of the LAI inversions from multi-sensor dataset in this study over 146 field measurements was 0.42. The validation accuracy of this study might influenced by the data quality and the values of input parameters. LAI inversions were greatly affected by the accuracy of HJ1/CCD data preprocessing, particularly for the heavily cloud-contaminated images, which leading to reflectance overcorrect for these images. Moreover, the background reflectance and pure vegetation reflectance extracting from various satellite images, such as HJ1/CCD, PROBA/CHRIS and Hyperion remote sensing data, were different, which was leading to the uncertainty of LAI retrievals.

5. Conclusions

The networking of multiple sensors is an efficient method to increase the observations from high spatial resolution remote sensing data in specific periods. This study explores an LAI inversion method based on a multi-sensor dataset generated combining HJ1/CCD and Landsat8/OLI from June to August 2013 in the middle reach of the Heihe River Basin, China. Considering the differences among various sensors, a data quality control system was introduced into the algorithm to select the valid observations. The inversion algorithm based on a unified model and biome-specific look-up tables was developed to generate the LAI products with 30 m spatial resolution and a 10-day temporal resolution. The analysis and validation results showed that:

(1) For the 10-day temporal resolution, the average valid observations increase from one based on single sensor to over three based on multiple sensors. The network of multiple sensors significantly improves the feasibility of generating 30 m remote sensing LAI products and their temporal resolution.

(2) Because of the observation complementation from different sensors, the proportion of valid LAI inversions significantly increased from 6.4% to 49.7% for single sensor to 75.9% for multi-sensor datasets.

(3) LAI retrieved from the multi-sensor dataset shows better agreement with the field measurements (R^2 is 0.90, and RMSE is 0.42) than LAI inversions from the single sensor. The temporal profiles of LAI inversions were relatively smooth, and the RMSE for most of the sampling plots were lower than 0.5.

The network of multiple sensors with 30 m spatial resolution can generate LAI products with reasonable accuracy and a meaningful temporal resolution. However, the satellite sensors involved in this study only included the Landsat8/OLI and HJ1/CCD data, while the experimental period is only one year. The limitation of the study area and data sources hindered the characteristic analysis of the multi-sensor dataset. Many more satellite observations with broader spatial and temporal resolutions will be required for further research.

Acknowledgments

This work was supported by National High Technology Research and Development Program of China (No. 2012AA12A304), Chinese Academy of Sciences Action Plan for West Development Project under Grant (No. KZCX2-XB3-15-2), National Natural Science Foundation of China (No. 41271366, No. 91325105, No. 41401393), CAS/SAFEA International Partnership Program for Creative Research Teams (No. KZZD-EW-TZ-09), and Key Laboratory of Satellite Mapping Technology and Application, National Administration of Surveying, Mapping and Geoinformation (No. KLAMTA-201409). The authors are grateful to Professor Qu Yonghua of Beijing Normal University for supplying the WSN LAI field measurements and the LAI-2200 field measurements near the EC towers and WSN stations.

Author Contributions

Jing Li, Qinhuo Liu and Jing Zhao conceived and designed the experiments; Wenjie Fan produced the LAI inversion algorithm based on a unified model; Bo Zhong and Shanlong Wu accomplished the multi-sensor data preprocessing; Le Yang and Yelu Zeng produced the data selection; Baodong Xu and Gaofei Yin provided the LAI field measurements.

Conflicts of Interest

The authors declare no conflict of interest.

References

1. Chen, J.M.; Black, T.A. Measuring leaf area index of plant canopies with branch architecture. *Agric. For. Meteorol*. **1991**, *57*, 1–12.
2. Chen, J.M.; Black, T.A. Defining leaf area index for non-flat leaves. *Plant Cell Environ*. **1992**, *15*, 421–429.
3. Fang, H.; Liang, S.; Kuusk, A. Retrieving leaf area index using a genetic algorithm with a canopy radiative transfer model. *Remote Sens. Environ*. **2003**, *85*, 257–270.
4. Chen, J.M.; Pavlic, G.; Brown, L.; Cihlar, J.; Leblanc, S.; White, H.; Hall, R.; Peddle, D.; King, D.; Trofymow, J. Derivation and validation of Canada-wide coarse-resolution leaf area index maps using high-resolution satellite imagery and ground measurements. *Remote Sens. Environ*. **2002**, *80*, 165–184.
5. Wan, H.; Wang, J.; Xiao, Z.; Li, L. Generating the high spatial and temporal resolution LAI by fusing MODIS and ASTER. *J. Beijing Norm. Univ. (Nat. Sci.)* **2007**, *43*, 303–308. (In Chinese)
6. Weiss, M.; Baret, F. Evaluation of canopy biophysical variable retrieval performances from the accumulation of large swath satellite data. *Remote Sens. Environ.* **1999**, *70*, 293–306.
7. Fassnacht, K.S.; Gower, S.T.; MacKenzie, M.D.; Nordheim, E.V.; Lillesand, T.M. Estimating the leaf area index of north central Wisconsin forests using the Landsat Thematic Mapper. *Remote Sens. Environ*. **1997**, *61*, 229–245.
8. Fernandes, R.; Butson, C.; Leblanc, S.; Latifovic, R. Landsat-5 TM and Landsat-7 ETM+ based accuracy assessment of leaf area index products for Canada derived from SPOT-4 VEGETATION data. *Can. J. Remote Sens*. **2003**, *29*, 241–258.
9. Tian, Q.J.; Jin, Z.Y. Research on calculation and spatial scaling of forest leaf area index from remote sensing image. *Remote Sens. Inf*. **2006**, 5–11.
10. Zhu, G.L.; Ju, W.M.; Chen, J.M.; Fan, W.Y.; Zhou, Y.L.; Li, X.F.; Li, M.Z. Forest canopy leaf area index in Maoershan Mountain: Groundmeasurement and remote sensing retrieval. *Chin. J. Appl. Ecol*. **2010**, *21*, 2117–2124.
11. Deng, F.; Chen, J.M.; Plummer, S.; Chen, M.; Pisek, J. Algorithm for global leaf area index retrieval using satellite imagery. *IEEE Trans. Geosci. Remote Sens*. **2006**, *44*, 2219–2229.
12. Masson, V.; Champeaux, J.-L.; Chauvin, F.; Meriguet, C.; Lacaze, R. A global database of land surface parameters at 1-km resolution in meteorological and climate models. *J. Clim*. **2003**, *16*, 1261–1282.
13. Knyazikhin, Y.; Glassy, J.; Privette, J.; Tian, Y.; Lotsch, A.; Zhang, Y.; Wang, Y.; Morisette, J.; Votava, P.; Myneni, R. *Modis Leaf Area Index (LAI) and Fraction of Photosynthetically Active Radiation Absorbed by Vegetation (FPAR) Product (Mod15) Algorithm Theoretical Basis Document*; Theoretical Basis Document; NASA Goddard Space Flight Center: Greenbelt, MA, USA, 1999.

14. Baret, F.; Hagolle, O.; Geiger, B.; Bicheron, P.; Miras, B.; Huc, M.; Berthelot, B.; Niño, F.; Weiss, M.; Samain, O. LAI, fAPAR and fCover CYCLOPES global products derived from VEGETATION: Part 1: Principles of the algorithm. *Remote Sens. Environ*. **2007**, *110*, 275–286.
15. Ganguly, S.; Schull, M.A.; Samanta, A.; Shabanov, N.V.; Milesi, C.; Nemani, R.R.; Knyazikhin, Y.; Myneni, R.B. Generating vegetation leaf area index earth system data record from multiple sensors. Part 1: Theory. *Remote Sens. Environ*. **2008**, *112*, 4333–4343.
16. Knyazikhin, Y.; Martonchik, J.; Myneni, R.; Diner, D.; Running, S. Synergistic algorithm for estimating vegetation canopy leaf area index and fraction of absorbed photosynthetically active radiation from MODIS and MISR data. *J. Geophys. Res. Atmos*. **1998**, *103*, 32257–32275.
17. Gascon, F.; Gastellu-Etchegorry, J.P.; Leroy, M. Using multi-directional high-resolution imagery from POLDER sensor to retrieve leaf area index. *Int. J. Remote Sens*. **2007**, *28*, 167–181.
18. Baret, F.; Weiss, M.; Lacaze, R.; Camacho, F.; Makhmara, H.; Pacholcyzk, P.; Smets, B. GEOV1: LAI and FAPAR essential climate variables and FCOVER global time series capitalizing over existing products. Part 1: Principles of development and production. *Remote Sens. Environ*. **2013**, *137*, 299–309.
19. Liang, S.; Zhao, X.; Liu, S.; Yuan, W.; Cheng, X.; Xiao, Z.; Zhang, X.; Liu, Q.; Cheng, J.; Tang, H. A long-term Global LAnd Surface Satellite (GLASS) data-set for environmental studies. *Int. J. Digit. Earth*. **2013**, *6*, 5–33.
20. Xiao, Z.; Liang, S.; Wang, J.; Chen, P.; Yin, X.; Zhang, L.; Song, J. Use of general regression neural networks for generating the GLASS leaf area index product from time-series MODIS surface reflectance. *IEEE Trans. Geosci. Remote Sens*. **2014**, *52*, 209–223.
21. Mousivand, A.; Menenti, M.; Gorte, B.; Verhoef, W. Multi-temporal, multi-sensor retrieval of terrestrial vegetation properties from spectral–directional radiometric data. *Remote Sens. Environ*. **2015**, *158*, 311–330.
22. Wan, H.W. Surface Parameters Inversion from Multi-Source Remote Sensing Data Fusion Study. Ph.D Thesis, Beijing Normal University, Beijing, China, 2007.
23. Liang, S.; Zhang, X.; Xiao, Z.; Cheng, J.; Liu, Q.; Zhao, X. *Global Surface Energy Budget and Ecosystem Variables* (*Glass*) *Product Algorithm, Validation and Analysis*; Higher Education Press: Beijing, China, 2014. (In Chinese)
24. Ganguly, S.; Nemani, R.R.; Zhang, G.; Hashimoto, H.; Milesi, C.; Michaelis, A.; Wang, W.; Votava, P.; Samanta, A.; Melton, F. Generating global leaf area index from landsat: Algorithm formulation and demonstration. *Remote Sens. Environ*. **2012**, *122*, 185–202.
25. Wan, H.W.; Wang, J.; Liang, S.; Qin, J. Combine MODIS and MISR data to retrieval LAI. *Spectrosc. Spectr. Anal*. **2009**, *29*, 3106–3111.
26. Hagolle, O.; Lobo, A.; Maisongrande, P.; Cabot, F.; Duchemin, B.; De Pereyra, A. Quality assessment and improvement of temporally composited products of remotely sensed imagery by combination of VEGETATION 1 and 2 images. *Remote Sens. Environ*. **2004**, *94*, 172–186.
27. Morton, D.C.; Nagol, J.; Carabajal, C.C.; Rosette, J.; Palace, M.; Cook, B.D.; Vermote, E.F.; Harding, D.J.; North, P.R. Amazon forests maintain consistent canopy structure and greenness during the dry season. *Nature* **2014**, *506*, 221–224.
28. Ju, J.; Roy, D.P.; Shuai, Y.; Schaaf, C. Development of an approach for generation of temporally complete daily nadir MODIS reflectance time series. *Remote Sens. Environ*. **2010**, *114*, 1–20.

29. Zhang, Y.H. HJ1-CCD Cross Radiometric Calibration. Master Themes, Shandong University of Science and Technology, Qingdao, China, 2011.
30. Leblanc, S.G.; Chen, J.M.; Cihlar, J. NDVI directionality in boreal forests: A model interpretation of measurements. *Can. J. Remote Sens*. **1997**, *23*, 369–380.
31. Walter, E.; Privette, J.; Cornell, D.; Mesarch, M.A.; Hays, C. Relations between directional spectral vegetation indices and leaf area and absorbed radiation in alfalfa. *Remote Sens. Environ*. **1997**, *61*, 162–177.
32. Chen, J.; Menges, C.; Leblanc, S. Global mapping of foliage clumping index using multi-angular satellite data. *Remote Sens. Environ*. **2005**, *97*, 447–457.
33. Yan, B.; Xu, X.; Fan, W. A unified canopy bidirectional reflectance (BRDF) model for row ceops. *Sci. China Press*. **2012**, *42*, 411–423.
34. Fan, W.; Xu, X.; Liu, X.; Yan, B.; Cui, Y. Accurate LAI retrieval method based on PROBA/CHRIS data. *Hydrol. Earth Syst. Sci*. **2010**, *14*, 1499–1507.
35. Fan, W.; Yan, B.; Xu, X. Crop area and leaf area index simultaneous retrieval based on spatial scaling transformation. *Sci. China Earth Sci*. **2010**, *53*, 1709–1716.
36. Li, X.; Li, X.W.; Li, Z.Y.; Ma, M.G.; Wang, J.; Xiao, Q.; Liu, Q.; Che, T.; Chen, E.X.; Yan, G.J.; *et al*. Watershed allied telemetry experimental research. *J. Geophys. Res*. **2009**, *114*, doi:10.1029/2008JD011590.
37. Li, X.; Cheng, G.D.; Liu, S.M.; Xiao, Q.; Ma, M.G.; Jin, R.; Che, T.; Liu, Q.H.; Wang, W.Z.; Qi, Y.; *et al*. Heihe Watershed Allied Telemetry Experimental Research (HiWATER): Scientific objectives and experimental design. *Bull. Am. Meteorol. Soc.* **2013**, *94*, 1145–1160.
38. Cheng, G.D.; Li, X.; Zhao, W.Z.; Xu, Z.M.; Feng, Q.; Xiao, S.C.; Xiao, H.L. Integrated study of the water-ecosystem-economy in the Heihe River Basin. *Natl. Sci. Rev.* **2014**, *1*, 413–428.
39. USGS. Earthexplorer. Available online: http://earthexplorer.usgs.gov/ (accessed on 18 February 2015).
40. China Centre for Resources Satellite Data and Application. Available online: http://www.cresda.com/n16/index.html (accessed on 18 February 2015).
41. Zhong, B.; Li, H.; Shan, X.; Mu, X.; Wu, H.; Chen, X.; Liu, Y. *Architecture of Multisource Data Processing System* (*ADPS*); No. 2012AA12A304; Institute of Remote Sensing and Digital Earth, Chinese Academy of Sciences: Beijing, China, 2014.
42. Zhong, B.; Zhang, Y.; Du, T.; Yang, A.; Lv, W.; Liu, Q. Cross-calibration of HJ-1/CCD over a desert site using Landsat ETM imagery and ASTER GDEM product. *IEEE Trans. Geosci. Remote Sens*. **2014**, *52*, 7247–7263.
43. Shan, X.J.; Tang, P.; Hu, C.M.; Tang, L.; Zheng, K. Automatic geometric precise correction technology and system based on hierarchical image matching for HJ-1A/B CCD images. *J. Remote Sens*. **2014**, *2*, 254–266.
44. Zhong, B. Improved estimation of aerosol optical depth from Landsat TM/ETM+ imagery over land. In Proceedings of 2011 IEEE International Geoscience and Remote Sensing Symposium (IGARSS), Vancouver, BC, Canada, 24–29 July 2011; pp. 3304–3307.
45. Zhong, B.; Wu, S.; Yang, A.; Liu, Q. An improved aerosol optical depth retrieval algorithm for moderate to high spatial resolution optical remotely sensed imagery. *IEEE Trans. Geosci. Remote Sens.* 2015. (Under Review).

46. Zeng, Y.; Li, J.; Liu, Q.; Qu, Y.; Huete, A.R.; Xu, B.; Yin, G.; Zhao, J. An optimal sampling design for observing and validating long-term leaf area index with temporal variations in spatial heterogeneities. *Remote Sens*. **2015**, *7*, 1300–1319.
47. Chen, B.; Coops, N.C.; Fu, D.; Margolis, H.A.; Amiro, B.D.; Black, T.A.; Arain, M.A.; Barr, A.G.; Bourque, C.P.A.; Flanagan, L.B.; *et al*. Characterizing spatial representativeness of flux tower eddy-covariance measurements across the Canadian Carbon Program Network using remote sensing and footprint analysis. *Remote Sens. Environ*. **2012**, *124*, 742–755.
48. Qu, Y.; Wang, J.; Dong, J.; Jiang, F. Design and experiment of crop structural parameters automatic measurement system. *Trans. Chin. Soc. Agric. Eng*. **2012**, *28*, 160–165.